FEATURE ARTICLE

Nanocrystal Self-Assemblies: Fabrication and Collective Properties

M. P. Pileni

Laboratoire LM2N, ESA CNRS 7070, Université P. et M. Curie (Paris VI), BP 52, 4 place Jussieu, 75252 Paris Cedex 05, France

Received: October 25, 2000

In this feature article, the methods of obtaining various mesostructures made of nanocrystals are described. With silver and silver sulfide, the nanocrystals are able to self organize in 2D and 3D super lattices to form "supra" crystals. With cobalt and ferrites nanocrystals, it has been possible to make ribbons, dots, or labyrinths. These mesostructures present new physical properties differing from those of the isolated nanocrystal and from those of the bulk phase. Collective optical, magnetic, and transport properties are demonstrated. By applying a magnetic field during the deposition process of nanocrystals, the easy axes of the particles are oriented along the direction of the applied field, inducing again the collective magnetic properties.

I. Introduction

Self-assembled nanocrystals have attracted an increasing interest over the last five years.[1−41] The level of research activity is growing seemingly exponentially, fueled in part by the observation of physical properties that are unique to the nanoscale domain. The first two-dimensional (2D) and three-dimensional (3D) superlattices were observed with Ag_2S and CdSe nanocrystals.[1,2,5,10] Since then, a large number of groups have succeeded in preparing various self-organized lattices of silver,[6,11−14,20,23−26] gold,[3,4,7,8,14−17,27−31] cobalt,[21,32] and cobalt oxide.[18,19] With the exception of CdSe[2] and cobalt[21,32] nanocrystals, most superlattice structures have been formed from nanocrystals whose surfaces are derivatized with alkanethiols.

If the experimental conditions of nanocrystal deposition are varied, a variety of organized structures have been achieved. For example, when silver,[13,27] gold,[3] CdS,[33] and barium ferrite[37] nanocrystals are deposited on a substrate, circular domains of monolayer nanocrystal coverage are observed, surrounded by regions of bare substrate. These phenomena were attributed to either wetting[3,13,27,33] or magnetic[37] properties. Under other deposition conditions, large "wires" composed of silver nanoparticles have been observed,[23] in which the degree of self-organization varies with the length of the alkyl chains coating the particles.[22]

It has been demonstrated that three-dimensional superlattices of nanocrystals are often organized in a face-centered cubic (FCC) structure.[1,2,5,10,11,20] In other cases, the particles pack in a hexagonal lattice.[9,12]

Interestingly, it has been recently demonstrated that the physical properties of silver,[20,34] cobalt,[21,3,35,39] and ferrite[40,41] nanocrystals organized in 2D and/or 3D superlattices differ from those of isolated nanoparticles. These changes in the physical properties are due to the close vicinity of nanocrystals at a given distance between each other. Such collective properties are attributed to dipole−dipole interactions. Furthermore, the electron transport properties drastically change with the nanocrystal organization.[36,37]

In this feature article, we report data obtained in our laboratory and others. First we focus on the fabrication modes of self-assemblies in 2D and 3D superlattices. Then we will present collective optical and magnetic properties. The paper ends with electronic transport processes.

II. Fabrication

At the end of synthesis, the nanocrystals are coated with dodecanethiol (except when otherwise specified). The various syntheses are described in The Appendix.

For 2D and 3D superlattices, the deposition procedure, nanocrystal concentration, substrate and alkyl chain length used to coat the nanocrystals play key roles.

II.1. Drop of Nanocrystal Dispersed in Solution Deposited under Air.[1,5,11,21,22,42] A drop of the solution containing silver sulfide nanocrystals is deposited on HOPG substrate with a filter paper underneath. The solution migrates from the substrate to the filter paper, and after a few seconds, the solvent is totally evaporated. At low concentration, islands made of self-assembled nanocrystals are observed (Figure 1A). When the concentration is increased (particle volume fraction, $\phi = 0.01\%$), monolayers made of nanocrystals are obtained over a very large domain (50 μm) (Figure 1B). The nanocrystals are organized in a compact hexagonal network with an average distance between particles of 1.8 nm. The monolayer formation is obtained for various nanocrystal sizes (from 2 to 6 nm). Similar data were obtained with silver[11,20] and cobalt[21,32] nanocrystals. Figure 2A shows the scattering electron microscopy (SEM) pattern. The gray region corresponds to 6 nm Ag_2S nanocrystal monolayers, and the darkest region is attributed to a hole in and outside the monolayers. The brightest regions correspond to 3D aggregates having somewhat oblate shapes with widths from 4 to 8 μm and heights less than 1 μm. Holes also occur within the large monolayer regions. The high-resolution atomic force microscopy (AFM) images show a flat and compact plain region. The Ag_2S nanocrystals are organized in local hexagonal
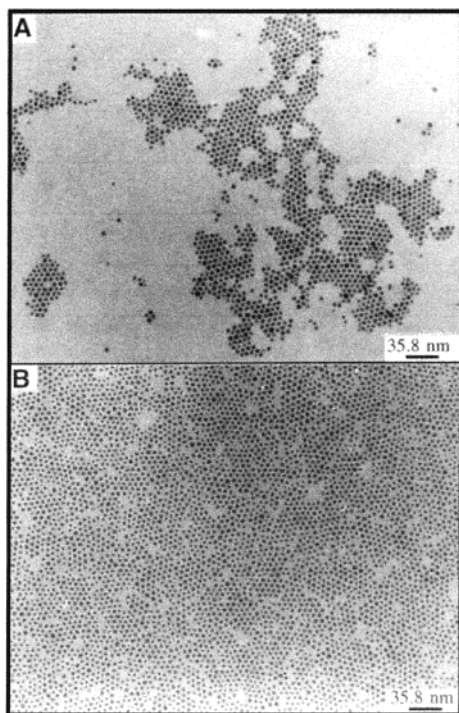
Figure 1. TEM images of a monolayer of 5.8 nm diameter silver sulfide nanocrystals deposited on amorphous carbon, observed at various nanocrystal concentrations.
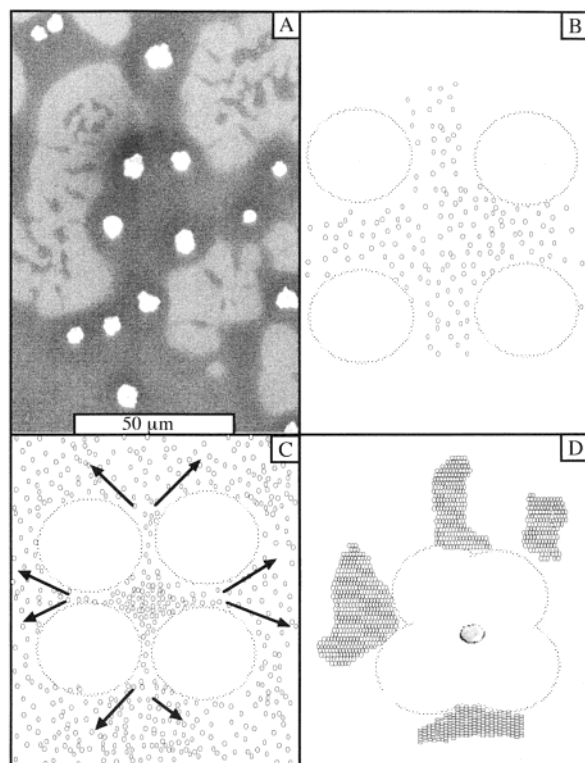

Figure 3. TEM image of 3D aggregate made of 5.8 nm silver sulfide nanocrystals.

Figure 2. (A) SEM image of 5.8 nm diameter silver sulfide nanocrystals deposited on HOPG (from a 10^{-6} M hexane solution at T = 20 °C). (B−D) Schematics of mono- and multilayer formation of nanocrystals as a result of solvent bubble growth and coalescence.

network domains with an 8 nm average center-to-center distance of the particles. Given the diameter of the nanocrystals (determined from TEM images), the average particle-to-particle separation is about 2 nm. The superlattice structures seen in the TEM, SEM, and AFM images above can be rationalized on the basis of interparticle, and particle−substrate, and
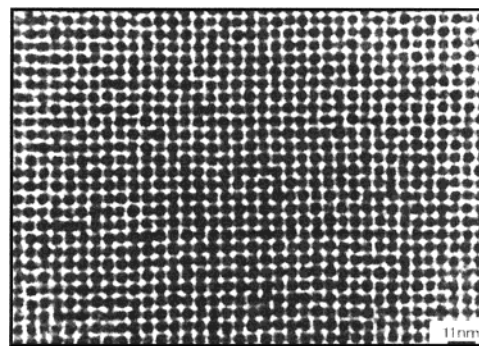
solvent−substrate (wetting) interactions. Recent work in our laboratories has shown that the attractive force between two Ag_2S nanocrystals is 1.8×10^{-6} dynes. The force between an Ag_2S nanocrystal and the HOPG substrate is repulsive (-3.7×10^{-6} dynes). Significantly, the heptane solvent on HOPG forms a nonzero contact angle (5−10°), which means that as evaporation occurs, the solvent film becomes unstable and droplets begin to form. The dynamics of these droplets play a key role in the evolution of Ag_2S nanocrystal assembly on HOPG. Consider the sketches in Figure 2B−D accompanying the SEM images in Figure 2A. Immediately after the solution containing the nanocrystals is deposited on the substrate, the solvent begins to evaporate and droplets form. The Ag_2S nanocrystals themselves are fully solvated by the heptane, which prevents their assembly into dense structures. As the droplets grow and begin to merge, some of the Ag_2S nanocrystals (which are still mobile because of the thin solvent layer present on the HOPG surface) are expelled away from the merge center (see arrows in Figure 2B). These dressed particles form compact monolayer islands, whose density increases after all of the solvent evaporates and interdigitation of the alkyl chains on the Ag_2S nanocrystal occurs. Other particles are caught in the center of the droplet merge point. The pressure exerted on these particles by the droplet menisci is large, and while a monolayer initially forms, continued droplet coalescence engenders the formation of a 3D structure (Figure 2D). This process may be viewed as analogous to the collapse of Langmuir films when the lateral pressure on the monolayer is too high. The three-dimensional structure of dressed particles dries out as the solvent evaporates, and thus, interdigitation of the particles alkyl chain coating occurs in 3D instead of 2D. The sizes of the 3D aggregates of Ag_2S are similar, which implies that the merge regions between growing solvent droplets are also similar in size. A key point implied by the scheme in Figure 2B−D is that the formations of monolayer and 3D aggregates occur essentially simultaneously. It should also be pointed out that very small 3D aggregates also form in the monolayer regions but via simple interparticle attraction rather than confinement and compression due to droplet growth. If HOPG is replaced with MoS_2 as the substrate, the monolayers are not as dense. This is attributed to strong attraction interactions between MoS_2 and Ag_2S nanocrystals inducing immediate sticking of the nanoparticles on the substrate before evaporation.[42] The compacity of monolayer on various substrates is governed by the relative ratio of particle−particle and particle−substrate Hamacker constant.[43]

The 3D aggregates of Ag_2S nanocrystals deposited on HOPG substrate are observed by SEM and TEM. Enhancement of the TEM pattern shows that the nanocrystals self-assemble in 4-fold symmetry (Figure 3). This can be attributed to the [001] plane

TABLE 1: Variation of the Average Distance (d_{pp}) between Alkanethiolate-Coated Nanocrystals Organized in a Hexagonal Network

	C_8	C_{10}	C_{12}	C_{14}
d_{pp} (nm)	1.4	1.6	1.75	1.8
$L_{cal} = 0.25 + 0.127n$ (nm)[a]	1.27	1.52	1.77	2.03

[a] n is the number of carbon atoms in the alkyl chain.

of an FCC lattice that can easily be seen. The center-to-center distance between two nanocrystals along the [010] plane is ca. 11 nm. The average particle diameter is 5.8 nm, and the shortest center-to-center distance is 7.8 nm, leaving a 2 nm edge-to-edge separation that is consistent with alkyl chain interdigitation. The supracrystal structure is stable under ambient conditions for a month. If the nanocrystal concentration in hexane is increased to 6×10^{18} particles per mL of solution, larger polycrystalline aggregates containing a large number of defects as dislocations are formed.[10] Similar 4-fold symmetry was obtained with silver nanocrystals.[11]

Instead of using dodecanethiol as a coating agent, we modified the length of the alkyl chain.[22] The nanocrystals formed in micelles cannot be extracted via surface derivatization with hexanethiol, octanethiol, or hexadecanethiol, (henceforth abbreviated C_6-, C_{16}-, and C_{18}- thiols, respectively). Thus they can only be removed from the oil environment along with the micelle-forming surfactant.

The intermediate chain length thiols (C_8-, C_{10}-, and C_{14}- thiols) appear to be the best suited for particle derivatization, extraction from the reverse micelles, and redispersion into hexane. TEM images of Ag_2S particles coated with these different thiols show that there is formation of self-organized hexagonal networks of the particles, whose interparticle spacings change systematically with alkanethiol chain length. However, the edge−edge separation distances do not correspond exactly to the distances one might expect from the alkyl chain lengths. Table 1 summarizes the interparticle spacings (edge−edge distances, henceforth referred to as d_{pp}) measured from TEM images. For comparison, the distances (L) calculated from the empirical equation of Bain et al.,[44] which assumes an all-trans zigzag conformation, are also shown. It is clear that the experimental d_{pp} values are considerably shorter than twice the chain length of the surface thioalkane groups. In the case of C_8- and C_{10}- thiol surface groups, d_{pp} is longer than L but shorter than $2L$. In the case of the C_{12}-thiol, d_{pp} is about equal to L. For C_{14}-thiol derivatized particles, d_{pp} is actually shorter than L. These trends can be explained by the change in chain conformation and the various defects that depend on chain length.[45] For example, the number of gauche defects near the particle surface decreases as the alkyl chain length increases. However, the incidence of gauche defects near the terminal (methyl) end of the chain increases with chain length. Hence, the shortest chains (C_8) behave almost as free alkanes and are thus not prone to 2D organization or interdigitation. As the chain length increases, interdigitation between alkyl chains on adjacent particles occurs, leading to a d_{pp} value that approaches the length of a single chain, L (C_{10}- and C_{12}-thiol systems). In the case of C_{14}-thiol surface groups, the increase in gauche defects near the chain terminal end allows pseudo rotational motion of the chain about the R−S bond axis. This explains why the d_{pp} value is smaller than L for the C_{14}-thiol system. There are two key observations in the study of alkanethiol chain length effects. First, the interparticle spacing, d_{pp}, is dependent on chain length, but the dependence is not linear. Second, using very short-chain alkanethiol groups (regardless of the difficulties inherent in the extraction step) to reduce interparticle spacing is not likely to
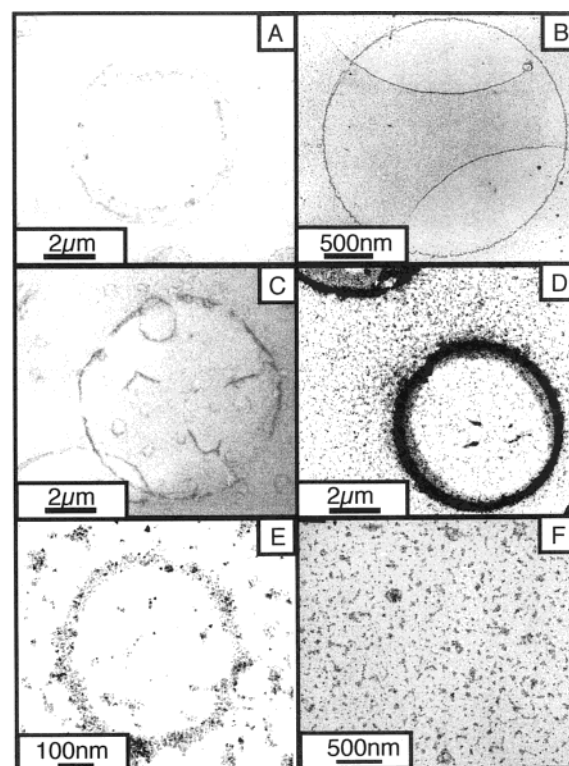

Figure 4. TEM images of silver sulfide (A), silver (B), cobalt (C), ferrite (D), cadmium sulfide (E), and silver (F). The nanocrystals are dispersed in hexane (A−E) and decane (F).

yield successful results. Short-chain compounds simply are not prone to 2D assembly and behave more as free alkanes.

For Ag_2S particles of virtually any size deposited with high concentration solutions (6×10^{18} particles per mL of solution) on amorphous carbon, large aggregates are formed. Nanocrystals coated with C_8- and C_{10}-thiols form well-faceted aggregates with 4-fold symmetry, as observed for the C_{12}-thiol-coated nanocrystals (Figure 3). Conversely, C_{14}-thiol-coated Ag_2S nanocrystals do not form well-defined supracrystals. The difference in self-assembly behavior when C_{14} alkanethiols are used is related to the d_{pp} edge-to-edge spacing parameter discussed earlier. For the alkyl chain lengths shorter than C_{14}, the d_{pp} value is either similar to (for example, $n = 12$) or slightly longer ($8 \le n \le 12$) than the calculated chain length, assuming complete trans (zigzag) conformation. The interdigitation of alkyl chains in these systems leads to a dense packing of the nanocrystals, which in turn results in well-defined 3D lattices. In the case of the C_{14} alkyl chains, the small d_{pp} value implies strong interparticle van der Waals attraction, despite the presence of a large number of gauche defects and poor interdigitation. We therefore conclude that well-defined 3D supracrystals require both strong interparticle interactions and alkyl chain interdigitation.

II.2. Drop Deposition on HOPG Substrate with an Anticapillary Tweezer.[46,47] The nanocrystals are dispersed in a solvent and a 4 μL droplet is deposited on a TEM grid, maintained with an anticapillary tweezer. The droplet remains on its support until the solvent is totally evaporated (solvent cannot escape from the grid). The nanocrystals are dispersed in hexane and deposited under air. Figure 4A shows formation of rings instead of monolayers self-organized in a compact hexagonal network (Figure 1B). The major differences between these two patterns are due to the deposition process. Similar behavior is observed with spherical silver (Figure 4B), cobalt (Figure 4C), and ferrite (Figure 4D) and with flat triangular CdS
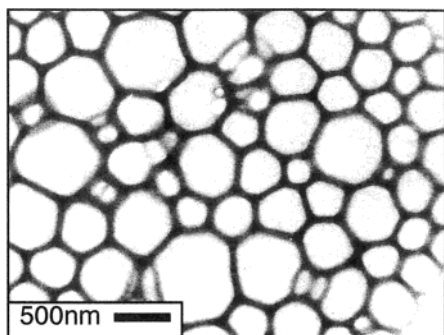
Feature Article

J. Phys. Chem. B, Vol. 105, No. 17, 2001 **3361**

Figure 5. Hexagonal patterns obtained with "concentrated" solutions of silver nanocrystals.

TABLE 2: Nanoparticle Size and Polydispersity

particles	diameter (nm)	polydispersity(%)
CdS	10 (size length)	—
Ag_{2S}	5.8	14
Ag	4.4	13
Cu	6.2	40
Co	5.1	35
citrate citratecoated γFe_2O_3	10.7	25
lauric acid coated γFe_2O_3	9.4	28

nanocrystals (Figure 4E). When nanocrystals dispersed in hexane are deposited on a TEM grid under a "quasi" saturated atmosphere, they are then randomly dispersed without any ring formation (Figure 4F). This is valid for the various nanocrystals described above. Such a change in the nanocrystal organization from rings to a random dispersion is due to the evaporation rate. In fact, the evaporation time (3 min) increases compared to that under air (30 s). Similar behavior with a random distribution of nanocrystals is obtained by replacing hexane by decane. Again, this confirms the influence of the evaporation time on the ring formation. Under air, the evaporation takes 25 and 2500 s in hexane and decane, respectively. Hence, formation of rings made of nanocrystals is related to the evaporation rate. This is strongly confirmed by the calculated values of the temperature gradient (ΔT) and Marangoni number (M_a). The estimated values of temperature gradient and Marangoni number of nanocrystals dispersed in hexane are 29 and 10^5 under air and 4.8 and 1.8×10^4 under saturated hexane, respectively. Similarly, when nanocrystals are dispersed in decane, the ΔT and M_a are 0.4 and 368, respectively. Hence, the decrease in the evaporation rate induces a decrease in the ΔT and M_a. This induces a decrease in the instabilities. When the evaporation time is reduced, the system equilibrates faster than the heat loss by the evaporation process. Under such conditions, instabilities disappear, and nanocrystals are randomly distributed on the carbon film. This means that formation of rings is related to the instabilities, induced by a fast evaporation process. Furthermore, it is not due to a dewetting-induced hole nucleation process of a thin film in a local equilibrium state because these structures do not appear when the system reaches equilibrium. The physical properties of the nanomaterials used (semiconductors, metals, and oxides) and their shape (spheres or triangles) are not related to ring formation. The formation of rings is related to neither the average size nor their size distribution (Table 2). However, the nanocrystals, characterized by a low size distribution, form rings made of nanocrystals self-assembled in hexagonal networks. Conversely, rings are formed by randomly dispersed nanocrystals when their size distribution is rather large. This is related to the patterns obtained by using the procedure described in II.1 (the grid is deposited on a paper sheet) where silver and silver sulfide are arranged in a hexagonal
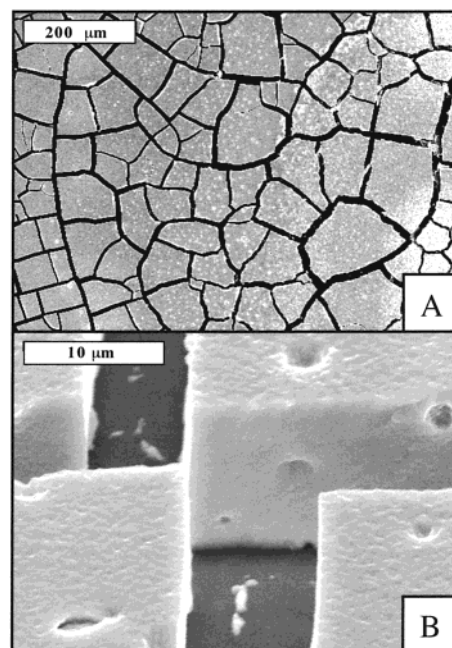

Figure 6. SEM patterns obtained from a HOPG substrate immersed in 200 mL of a highly concentrated silver colloidal solution (3×10^{-6} mol/L) and dried 9 h under a hexane vapor atmosphere: (A) at low magnification and (B) at higher magnifications and tilted by 45°.

network whereas cobalt and copper are not. It can thus be concluded that rings formed with nanocrystals having a low size distribution have a well-defined structure (compact hexagonal network). Conversely, when the size distribution of nanocrystals is rather large, the rings consist of randomly dispersed particles.

When particle concentration is increased, more complex organizations made of closely packed structures are observed on the TEM grid. Arrays of hexagonal patterns (Figure 5) are seen with the dark "walls" corresponding to nanocrystal aggregates whereas the bright regions correspond to low particle density areas. This is again obtained whatever the nature of nanocrystals. These structural changes are due to the increase in nanocrystal concentration because it is the only parameter which has been modified compared to that observed in Figure 4. These patterns are similar in shape to those observed in Bénard's experiment with liquid films and attributed to a Marangoni effect. This is consistent with theories where a concentration gradient induces an increase in the Marangoni number and, consequently, instabilities such as that observed for a temperature gradient. Again, as observed at low concentration, the TEM patterns totally differ with the deposition procedure. A hexagonal pattern is observed with an anticapillary tweezer, whereas a compact FCC structure made of nanoparticles is obtained by using the procedure described in II.1.

II.3. Deposition under Hexane Vapor.[48,49] The HOPG substrate is horizontally immersed in 200 μL of a high concentration of silver nanocrystals (3×10^{-6} mol/L). The substrate temperature, controlled using a thermocouple-based module, is fixed at 35 °C. Solvent evaporation takes place under a hexane vapor atmosphere which is not completely saturated. The evaporation time markedly increases compared to that under air, taking 9 h instead of few minutes. SEM shows a uniform large coverage. At the center of the substrate, the height of the deposition reaches a maximum, where small cracks and large aggregates are observed at higher magnification (Figure 6A). They are well separated by an average distance of 10 μm. The average surface area of the aggregates is deduced from that
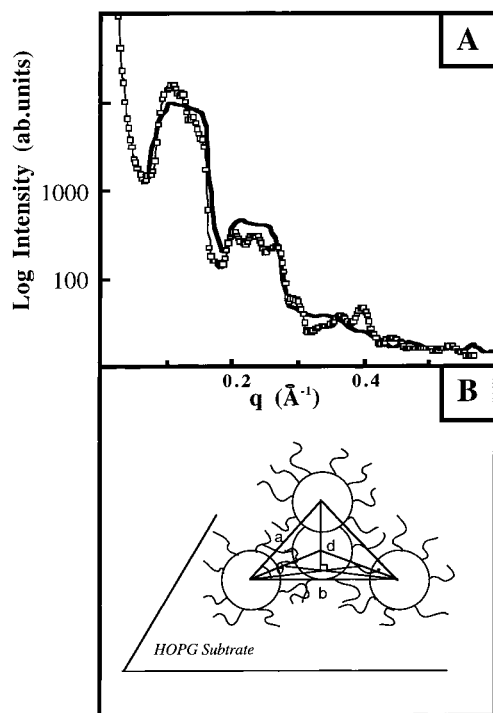
Figure 7. Experimental (—) and simulated (-O-) X-ray reflectograms of silver nanoparticle 3D superlattices (A). Sketch showing the stacking of silver nanocrystal monolayers (B).

Figure 8. SEM patterns obtained from HOPG substrates left in air, at room temperature, for 1 month (A) and 5 months (C). X-ray reflectograms of the "supra" crystals aged 1 month (C) and 5 months (D) under air.

measured of each aggregate on different parts of the graphite substrate. The average surface area is 2700 μm^2, and its distribution[50] is 0.4. The 3D structure is confirmed by tilting the sample by 45°, and this makes it possible to estimate that the average height of the aggregates in the center of the substrate is 15 μm (Figure 6B). In addition, the boundaries between blocks have straight edges, which is consistent with a crystalline structure. These broken edges, like the roughness of the aggregate surface, are a consequence of thermal stress. In fact, under evaporation, surface tensions are generated which create holes on the aggregate (Figure 6B).

X-ray diffraction measurements show two superlattice peaks. The large width of the peaks (Figure 7A) is rather surprising for a compact structure but is explained by assuming that each peak is due to a distribution of periods. The position of the peaks gives the period d. A simple model based on a minimal distance of 1.8 nm between nanocrystals and a varying angle θ of tetrahedrons (Figure 7B) is in agreement with the experimental data (Figure 7A). For the simulation, six different configurations corresponding to six various periods (d = 6.55, 6.1, 5.7, 5.2, 4.7, and 4.2 nm) are considered. Figure 7B gives two examples of such configurations. The mean period, deduced from the mean position of the peaks, is 5.6 nm, and it corresponds to the theoretical distance for a compact FCC or HCP structure with 6.8 nm distance between particle centers. The coherence of each period is larger than five layers. These period variations are attributed to differential solvent evaporation. The residual solvent not yet evaporated drives away the silver nanocrystals, thus inducing an increase in the particle—particle distance and variable periods. By changing the substrate temperature, we drastically change the shape of the "supra" crystal. The concentration of nanocrystals used and the presence or absence of hexane vapor are also important parameters.

This variation of periods is attributed to differential solvent evaporation. The residual solvent not yet evaporated drives away the silver nanoparticles that induces an increase of the distance
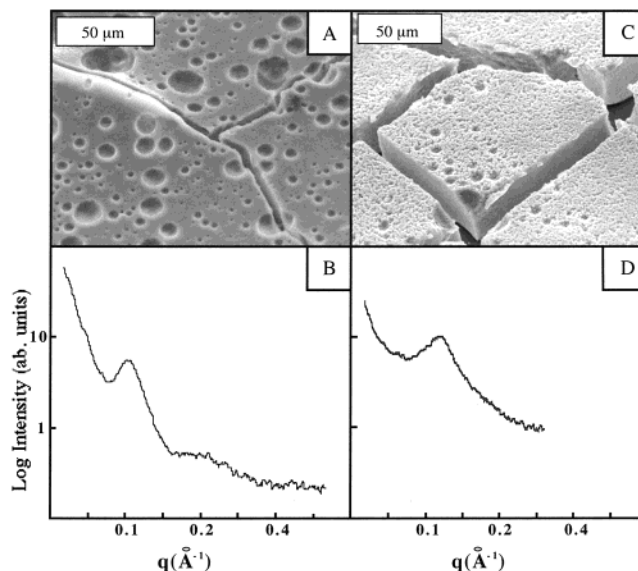
particle—particle and variable periods. Indeed, it has to be noted that the HOPG substrate is immersed in the colloidal solution and dried for 9 h at 35 °C under hexane vapor. After that, air is let into the sample at room temperature. Nevertheless, the residual solvent can remain inside the silver nanoparticles aggregates. This confirms data obtained by STM under vacuum, where monolayers of nanocrystals were visualized only after heating the substrate which induce the solvent desorption. In the present case, the "supra crystal" is left under the air, and the residual solvent takes long time to evaporate because the aggregates are very thick (around 15 m). The solvent is more easily evaporated near the surface of the aggregates than inside, explaining the increase in the surface roughness during the aging (Figure 8A,B). The X-ray diffraction experiments are carried out with 1 and 5 months old samples, where drastic changes in the morphology, the surface, and the structure are observed. The 1 month aged sample has two superlattice peaks with a strong decrease in the width ($\Delta q = 0.04$ Å^{-1}) compared to the sample immediately prepared (Figure 8C). The distribution of periods is narrower. The evaporation of the residual solvent has reduced the mean distance between the particles. The position of the peaks give a mean period of 6.1 nm, which is well inferior to the maximum period (6.55 nm) observed in the case of the sample immediately prepared. Nevertheless, the second-order peak is not as well defined, indicating a decrease in the organized structure. With the 5 months old sample, only one diffraction peak is observed (Figure 8D). It is shifted to the high q values, indicating large damage in the superlattice. The width of the peak is close to that of the peaks observed with the 1 month old sample, and its position gives a mean period of 5.3 nm. Thus only small periods d remain, and the distance particle—particle has strongly decreased. When the substrate is dipped in hexane, the nanocrystals are dispersed, and the substrate remains free of "supra" crystals. A drop of the solution containing the nanocrystals is deposited on a carbon grid. The TEM image shows monolayer organized in hexagonal network as obtained with fresh solution and agglomerate silver particles. The relative amount of coalesced particles increases with the "supra" crystal age. This permits the conclusion that the roughness observed when the "supra" crystals aged is due to
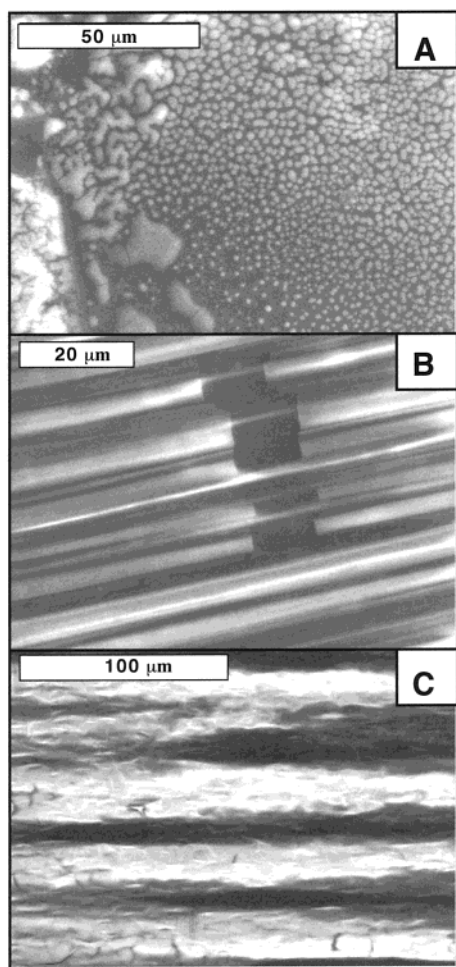
Feature Article

J. Phys. Chem. B, Vol. 105, No. 17, 2001 **3363**

Figure 9. SEM patterns of cobalt superlattices obtained by evaporating 200 mL of a solution of cobalt nanoparticles (5×10^{-7} M in particles) on HOPG substrates. The evaporation time is 12 h deposition without applied field (A) and with 0.56 T (B) and 0.27 T (C) applied field parallel to the substrate.

the coalescence of nanocrystals induced by desorption of thiododecane.

II.4. Nanocrystals Subjected to an Applied Magnetic Field during Deposition. *II.4.1. Cobalt Nanocrystals.*[51] Cobalt nanocrystals form 2D arrays with a hexagonal network.[21] However, it is not possible by increasing nanocrystal concentration to get 3D aggregates, as observed with silver and silver sulfide nanocrystals (Figure 9A). The observed film is made of aggregates without a defined shape dispersed or agglomerated on the substrate. To organize the nanocrystals, we used the following procedure: Freshly cleaved HOPG substrate is immersed in 200 μL of 4×10^{-7} M nanocrystals dispersed in hexane. The evaporation process, which takes 12 h, occurs under hexane vapor and produces a black magnetic film. When the applied magnetic field is parallel to the substrate during the deposition process, the nanocrystals assemble with the formation of large linear patterns along the field (Figure 9B,C). The average height of the film, determined by tilting the sample, is 2 μm. The film made of cobalt nanocrystals shows a large extent of corrugation with a quasiperiodic structure in the direction of the applied field. The patterns cover the overall HOPG substrate, and the height of the film remains similar for any applied field. However, the corrugation markedly changes with the strength of the applied field. The wavelength of the corrugation is defined as the average distance between two maxima on the film. When the applied field is 0.27 T, there is a rather rough surface with
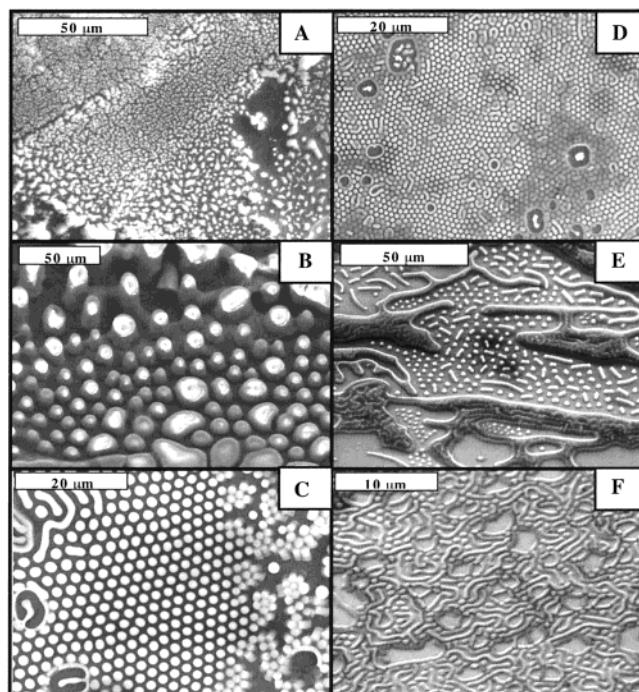

Figure 10. SEM patterns obtained by evaporating 200 mL of a concentrated solution of cobalt nanocrystals (4×10^{-7} M in particles) deposited under a magnetic field perpendicular to the HOPG substrate. The evaporation time is 12 h. The strength of the applied field is 0 (A), 0.01T (B); 0.27T (C); 0.45T (D); 0.60T (E) and 0.78T (F).

a corrugation wavelength of 38 μm, as shown in Figure 9C. On increasing the applied magnetic field to 0.56T, the wavelength shows a large decrease to 7 μm (Figure 9B), and the structures are sharper. Thus, the ordering and compacity of the corrugated film made of cobalt nanocrystals markedly increase with the strength of the applied film.

When the external applied magnetic field is perpendicular to the substrate, a large variety of mesostructures made of 8 nm cobalt nanocrystals depending on the strength of the field is observed (Figure 10). The addition of a hexane drop to the substrate totally destroys these structures, and the SEM pattern is similar to that observed in the absence of an applied magnetic field (Figure 9A). The UV spectrum and magnetic hysteresis loop of nanocrystals collected from the substrate and dispersed in hexane remain unchanged compared to those observed before deposition. From this, it is concluded that no coalescence takes place when nanocrystals form a 3D film. Whatever the superlattices are, the background of the sample is covered by multilayers made of 8 nm cobalt nanocrystals. The superlattices sit on the film, and the average film height, determined by tilting the sample, is around 3 μm. The shape of the structure markedly changes with the strength of the applied field: with no applied field, a large-scale SEM picture shows a very inhomogeneous structure (Figure 10A). At a very low applied field ($H = 0.01$), there are large dots, as shown in Figure 10B with a rather wide size distribution (Table 3). The average diameter and distance between dots are 11.7 and 14. 3 μm, respectively. When the sample is tilted, the height of the dots is evaluated to be, on average, 8 μm with a large polydispersity, 37%. Table 3 shows a rather large distribution in size and interdot distances. On increasing the applied magnetic field to 0.27T, we observed well-dispersed dots (Figure 10C). Enhancement of the SEM grid shows that these dots are organized in a well-defined hexagonal network (Figure 11). The average dot diameter is 1.75 μm with a size distribution of 5.3%, and the interdot distance is 2.4 μm

TABLE 3: Structure and Characteristics of the Cobalt Film Obtained by Evaporating 200 μL of a Concentrated Solution of Cobalt Nanocrystals (4×10^{-7} M in Nanocrystals) on HOPG Substrates at Various Perpendicular Fields

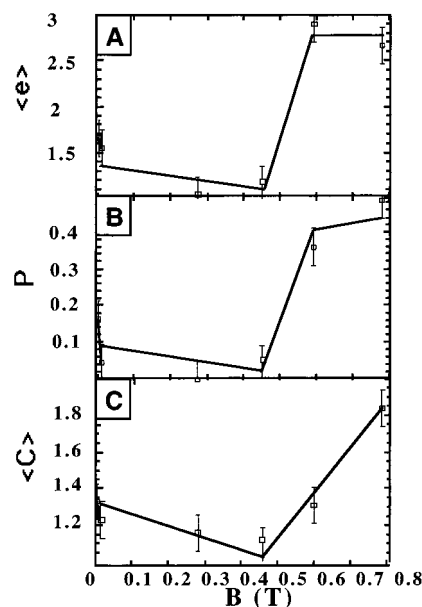| field (Teslas)	structure	diameter of dots (μm)	size distribution (%)	height (μm) (distribution)	interdots distances (core to core) μm
0	none	—	—	—	—
0.01	unorganized dots	11.7	25	8 (37%)	14.3
0.27	hexagonal network cylindrical dots	1.75	5	0.5 (21%)	2.40
0.45	hexagonal network of cylindrical dots	0.75	10	0.3 (17%)	1.1
0.60	worms, cylindrical dots and labyrinth	1.5	24	1.0 (83%)	—
0.78	labyrinth	0.6*	13	0.2 (39%)	—
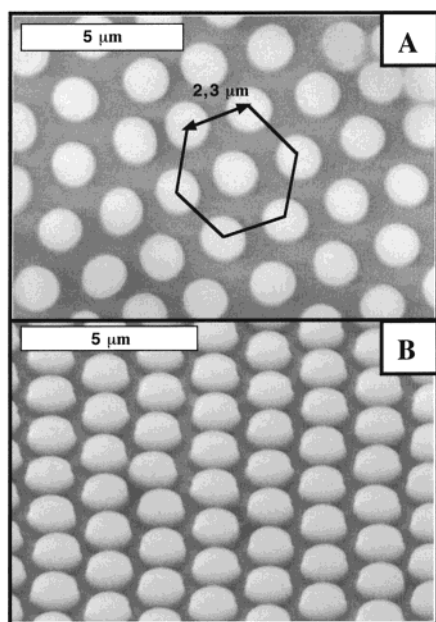
Figure 11. (A) SEM patterns at different magnifications of superlattices obtained on HOPG substrates, with an applied field of $H = 0.27$ T. The hexagonal network is visible. (B) Tilted SEM pattern showing the 3D structures. The deduced height is 1 μm for each pillar.

Figure 12. (A) Evolution of the average form factor $\langle e \rangle$, (B) the worm ratio P, and (C) the average complexity $\langle C \rangle$ with the intensity of the applied field during the deposition of the cobalt nanoparticles on the substrate.

(core to core). The 3D aggregate height is 0.5 μm. Figure 11 clearly shows well-defined columns with a very sharp interface. This could be due to a high order of nanocrystals in the superlattices. A further increase in the applied field to 0.45 T shows patterns similar to those observed under 0.27 T (Figure 10C). However, the average diameter and interdot distance are markedly reduced to 0.75 and 1.1 μm, respectively (Table 3). By applying a magnetic field of 0.60 T, we observed drastic changes. Figure 10E shows the presence of dots, wormlike and labyrinth structures. A further increase in the magnetic field to 0.78 T enables formation of a homogeneous labyrinth structure. At and above an applied magnetic field of 0.27 T, the height of the superlattices remains unchanged (0.5–1 μm). Hence, by applying a magnetic field during the cobalt nanocrystal deposition on a substrate, it is possible to form well-defined 3D superlattices. The structure is observed on a very large scale (up to 0.02 mm^2). To obtain more quantitative results, we use the same parameters as those developed for magnetorheological fluids:[52]
(i) The parameter e is the ratio of the end-to-end length to width. If $e > 2$, the superlattice is classified as wormlike. If $e = 1$, it is called dots, and if $1 < e < 2$, it is disklike.
(ii) P is the ratio of the number of worms to the total number of aggregates

$$P = N_{e=2}/N_{total}$$

(iii) $C = $ (perimeter of aggregates)/2×f7(π area of aggregates);

thus, the average complexity is defined as

$$\langle C \rangle = \times c2 C_i / N_{total}$$

Figure 12 shows the variation of these three parameters with the applied magnetic field. From data presented above, three behaviors are observed:
(i) Under a very low perpendicular applied field (H = 0.01T), there is a transition between agglomerate cobalt nanocrystals to disklike structures with a rather large size, shape, and interdot distance distribution.
(ii) In the 0.01 T < B < 0.47 T range, well-defined hexagonal patterns are observed. For a given applied field, the size and interdot distance are rather low. On increasing the applied field, the diameter and the distance between dots decrease. The latter evolves continuously with the reciprocal of the applied magnetic field.
(iii) At 0.47 T, the transition onset from columns, well-dispersed in a hexagonal network, to worms and labyrinths is observed. At and above 0.78 T, well-defined labyrinths are observed. The origin of the phenomenon is similar to that obtained with concentrated ferrofluids when they are subjected to an applied field:[53,54] for magnetorheological fluids, without an applied field, no structure is observed. Columns organized in hexagonal networks or labyrinth patterns are observed by applying a magnetic field perpendicular to the sample. The major difference between the experiments performed with magnetic fluids and the present data is based in the experimental conditions under which such structures are observed: These structures are

Feature Article

J. Phys. Chem. B, Vol. 105, No. 17, 2001 **3365**

observed when a perpendicular magnetic field is applied to a magnetic fluid characterized by a given particle volume fraction. They disappear when the applied field is turned off. In the present experiment, the particle volume fraction increases under evaporation progressively to reach a compact packing in the absence of solvent. The structures then remain unchanged when the applied field is turned off. From the shape of the patterns observed under both conditions, it is assumed that such changes have the same origin. In the present study, the substrate is immersed in a solution containing 8 nm coated cobalt nanocrystals dispersed in hexane. The interface between hexane vapor and the nanocrystal solution is dynamic and spatially modulated as a result of the competition between the magnetic interaction and the surface tension. In absence of external constraints, the amplitudes and the phases of this wavelike deformation are rather weak. Applying a low magnetic field results in interactions between nanocrystals. This induces changes in the wave amplitudes and the nonlinear effects lead to chaotic dynamics in which many degrees of freedom are active. The application of a magnetic field increases the interface fluctuations, and the film is disrupted along the field direction. There is intense competition between the intrinsic surface tension and the magnetic interaction energies. The first factor tends to decrease the instabilities, while the second acts in the opposite direction. The surface is then a superimposition of interacting waves. The surface tension of the interface tends to confine the nanocrystal solution in drops, whereas the dipolar forces push the ferrofluid apart. The magnetic interactions start to be predominant and favor column growth. The increase in the applied magnetic field value induces an increase in the wavelike deformations and then in the instabilities. If it is assumed that the 3D superlattice growth takes place on the instabilities, the distance between them is expected to depend on the strength of the applied field. In fact, the interdistance of dots well-organized in hexagonal networks decreases with increasing the applied field, as observed (Table 3). When the applied field is high enough, the instabilities are well distributed over the film, and each dot tends to fuse with its neighbor to form wormlike and labyrinth structures.

II.4.2. Ferrite Nanocrystals.[40,41] The data described below are similar for $CoFe_2O_4$[55] and γFe_2O_3[56] nanocrystals. Ferrite nanocrystals are coated with citrate ions and dispersed in water with the same average size and distribution as those of nanocrystals of silver or silver sulfide and are deposited using the procedure described in II.1. By deposition of a drop on the TEM grid, we observe nanocrystals (Figure 13A). It can be noticed that they do not self-organize. The deposition procedure is changed as followed: Seven 10 μL drops of an aqueous solution containing 0.17wt. % nanocrystals are deposited on the HOPG substrate. The sample is or is not subjected to a given magnetic field. The drops remain on the substrate during the evaporation process. By controlling the nanocrystal concentration of the magnetic fluid, we deposited the same amount of nanocrystal on the substrate. With no field, a large coverage of the substrate is observed (Figure 13B). The cracked film is made of highly compact spherical agglomerates, and its thickness, determined by tilting the sample, is about 2 μm (insert Figure 13B). Deposition of a water drop on the SEM grid destroys this agglomeration. The nanocrystals are then collected, and a drop of solution is deposited on a TEM grid. The pattern is similar to that shown in Figure 13A. This clearly indicates that the patterns shown in Figure 13B correspond to agglomerates made of spherical nanocrystals without any coalescence. It can be noticed that the SEM pattern obtained in absence of applied magnetic field markedly differs (Figure 13B) from that observed
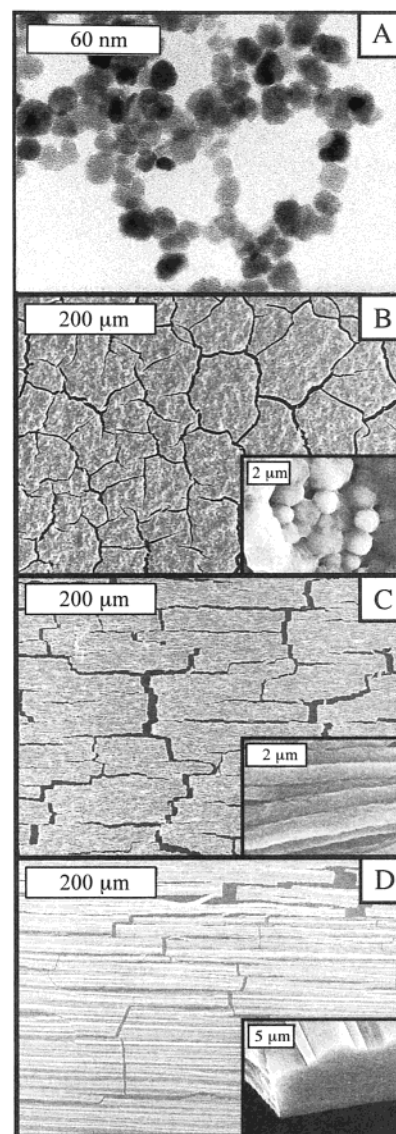

Figure 13. (A) TEM pattern of a drop of maghemite magnetic fluid deposited on a grid. SEM patterns of ferrite nanocrystals deposited on a HOPG subjected to an applied field of 0 T (B), 0.01 T (C), and 1.8 T (D), inserted corresponding to the SEM pattern tilted by 45° (B).

for cobalt nanocrystals (Figure 9A). When a magnetic field parallel to the substrate is applied during the deposition process, the SEM patterns markedly change. For any applied field value, the nanocrystals are organized in ribbons with a rather constant film thickness (4−5 μm) (Figure 13C,D). However some differences are observed: at low applied field ($H = 0.01$ T), the roughness of the sample is rather large (Figure 13C). When the sample is tilted (insert Figure 13C), the ribbons are porous and poorly aligned. A progressive increase in the applied field favors the large coverage characterized by a linear orientation of the nanocrystals along the applied field direction. A very regular, needlelike structure stretched in the magnetic field direction is observed. At and above the 0.05 T applied field, the nanocrystal organization is highly homogeneous (Figure 13D). When the sample is tilted, this organization is seen to consist of superimposed tubes made of nanocrystals (insert Figure 13D)

III. Collective Properties

III.1. Optical Properties.[20,34,35] In the UV−visible spectral range, the broad absorption bands of metal nanocrystals are due
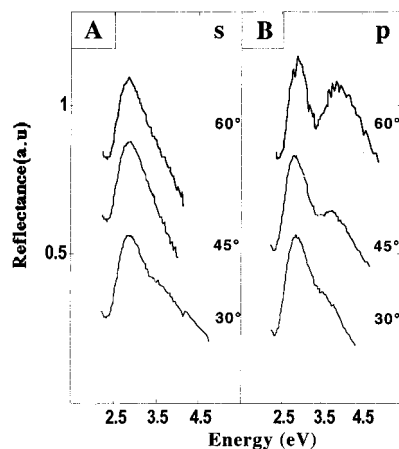
Figure 14. UV−vis polarization absorption spectra of 2D hexagonal lattice of 5 diameter silver nanocrystals on HOPG substrate: (A) s-polarization and (B) p-polarization. Numbers next to curve indicate incidence angle.

to plasmon resonance excitations or interband transitions. The spectra of dilute solutions of metal nanocrystals can be modeled quite well with Mie Theory.[57−63] Both the experimental[20,64] and simulated[62,65] absorption spectra show a decrease in the plasmon resonance band intensity and an increase in bandwidth with decreasing particle size. The shape of the experimental peaks shapes is nearly Lorentzian, and discrepancies at higher energies are due to interband transitions in the experimental system 4d−5sp.[66] When silver nanocrystals are organized into a 2D lattice, the plasmon resonance peak is shifted to energies lower than that obtained for dilute solutions of isolated particles. The absorption spectra of dodecanethiol-coated 5 nm diameter silver nanoparticles in hexane solution before and after surface deposition and redispersion in hexane are similar. When the same nanocrystals are deposited in 2D and 3D, a spectral shift more pronounced in 3D than in 2D[20] is observed. Since the original hexane solution spectrum and that of the redispersed particles are virtually the same, the spectral shifts associated with the 2D and 3D assemblies must come from interparticle electromagnetic interactions and not from some physical or chemical transformation associated with their deposition. The bandwidth of the 2D plasmon resonance peak is ca. 1.3 eV, considerably larger than that of the particles in dilute solution (ca. 0.9 eV). Similar behavior is observed for silver nanocrystals of various sizes (from 3 to 8 nm). UV−vis polarization spectroscopy can reveal information about interparticle electromagnetic interactions. In s-polarization, the electric field vector is oriented parallel to the plane of the substrate at all incidence angles θ. Plasmon resonance modes with components polarized perpendicular to the plane of the substrate are not seen when the incident light is s-polarized.[67] On the other hand, p-polarized light, whose electric field is parallel to the plane of incidence, can probe plasmon resonance excitations whose components are either parallel or perpendicular to the substrate. For 2D assemblies of metal nanocrystals on planar substrates, p-polarized light is thus ideal for probing interparticle interactions.[68] Figure 14 shows the UV−vis polarization absorption spectra of a hexagonal 2D assembly of 5 nm silver nanocrystals on an HOPG substrate.[34] In s-polarization, the absorption spectra are virtually independent of incidence angle θ (Figure 14A) and show a plasmon resonance band centered at 2.9 eV, which is similar to that seen in isolated silver nanocrystals. The degree of band asymmetry is also similar to that seen in isolated particles. However, in p-polarization, a second band appears at higher energy as the incidence angle is increased (Figure 14B).
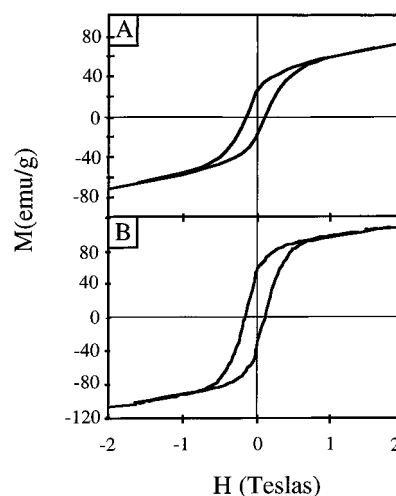

Figure 15. Hysteresis magnetization loops obtained at 3 K for cobalt nanocrystals. Dilute solution of 5.6 nm (A) and 8 nm (B) cobalt nanocrystals in hexane (0.01% volume fraction in hexane).

At $\theta = 60°$, the two peaks are well-defined: the first is close in energy (2.8 eV) to the absorption maximum for isolated particles (2.9 eV), but the second is centered at ca. 3.8 eV. We should note that these data are reproducible and are not sensitive to coverage effects. To determine if polarization spectra such as those shown in Figure 14B are due to a self-organized lattice, we conducted similar spectral studies on 5 nm silver nanocrystals randomly distributed on an HOPG substrate. In s-polarization at $\theta = 60°$, the UV−vis spectrum shows a single plasmon resonance band centered at 2.7 eV. With p-polarized light at the same incidence angle, the plasmon resonance band is split into two peaks, one slightly higher and one slightly lower in energy than the peak in the s-polarization spectrum. The TEM image shows that while the silver nanoparticle sizes are quite uniform, a few particles touch each other and perhaps even to the point of coalescence. This interaction may account for the peak splitting. However, the energy difference between the two peaks is very small compared to the case of the p-polarization spectrum of a hexagonal 2D lattice (Figure 14B). It can be concluded that the high-energy band at 3.8 eV in Figure 14B is due to the self-organization of the silver nanocrystals into a hexagonal network. The position of the peak can be explained in terms of local field effects. Each nanocrystal is subjected to the electric field of the incident light plus the dipolar fields of the particles in its vicinity. The calculated spectra for finite sized clusters under s- and p-polarization are in qualitative accord with the results presented here.

III.2. Magnetic Properties. *III.2.1. Cobalt Nanocrystals.*[21,32,35,69,70] Cobalt nanocrystals having an average size of 5.6[21] and 8 nm[70] self-assemble in 2D superlattices. However some nanocrystal deficiencies in the self-assembly are observed. The fraction of nanocrystal vacancies on the substrate is estimated to be 20%. The magnetization curve recorded at 3 K of 5.6 nm nanocrystals dispersed in hexane (0.01% in particle volume fraction) is smoother (Figure 15A) than that obtained under the same experimental conditions for 8 nm nanocrystals (Figure 15B). In both cases, saturation magnetization is not reached. It is estimated to be 110 and 120 emu/g for 5.6 and 8 nm, respectively (based on an extrapolation of H/M versus H). These values are significantly lower than that of the bulk phase ($M_s = 162$ emu/g). The large difference between the saturation magnetization of nanocrystals, M_s, and that of the bulk phase M_s(bulk) is attributed to the strong interactions between the carbonyl group of the coating agent and the cobalt atoms at the

Feature Article

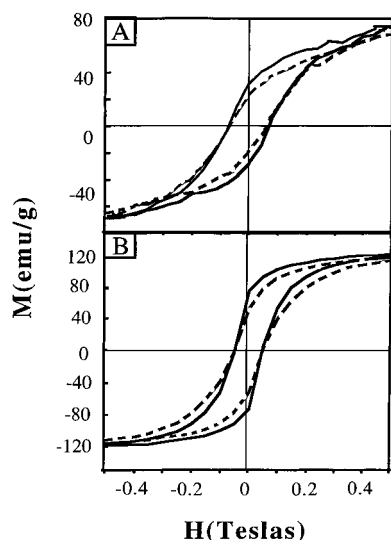*J. Phys. Chem. B, Vol. 105, No. 17, 2001* **3367**

Figure 16. (A) 5.6 nm and (B) 8 nm cobalt nanocrystals deposited on HOPG. Solid curve: magnetic field parallel to the substrate. Dashed curve: magnetic field perpendicular to substrate.

TABLE 4: Nanocrystal Diameters

nanocrystal diameter	$(M_r/M_s)_l$	$(M_r/M_s)_{par}$	$(M_r/M_s)_{per}$	γ_{theo}	γ_{exp}
5.6 nm		0.28	0.21	0.70	0.60
8 nm	0.51	0.60	0.40	0.60	0.66

particles surface. This is supported by the fact that adsorbed species on metal magnetic nanocrystals change the magnetization of the particles through the quenching of the surface atom contribution. This was calculated and observed for small nickel and NiPt clusters ($Ni_{38}Pt_6$) coated by CO ligands. Carbonyl ligands completely quench the magnetic moments of the nickel atoms at the cluster surface, leaving the inner-core metal atoms unaffected.[69] Magnetization curves for nanocrystals deposited on the substrate and subjected to fields either parallel or perpendicular to the substrate surface show clearly the change in the shape of the hysteresis loop with the orientation of the applied field relative to the substrate surface (Figure 16A,B). When the field is parallel to the surface, the hysteresis loop is more square than that corresponding to the nanocrystals dispersed in solution. Conversely, when the field is perpendicular to the surface, the hysteresis loop is smoother than that corresponding to the dispersed particles. For the two orientations of the field, saturation is reached at 2 T.

Under a parallel applied field, the saturation magnetization is reached at a larger value for 5.6 nm (Figure 16A) than for 8 nm (Figure 16B) nanocrystals. Table 4 gives the reduced remanence measured from magnetization curves when nanocrystals are either in liquid $(M_r/M_s)_l$ or deposited on a substrate. In the latter case reduced remanences recorded when the applied field is parallel, $(M_r/M_s)_{para}$, or perpendicular, $(M_r/M_s)_{perp}$, to the substrate are given in Table 4. Such changes in the magnetization curves of nanocrystals deposited on a substrate compared to those dispersed in a matrix are due either to exchange coupling between adjacent particles or to the long-range dipole coupling with a collective "flip" of the magnetic dipole. The exchange coupling can be excluded because the edge-to-edge separation (2 nm) between two nanocrystals is too large. Numerical calculations of magnetization curves versus the applied field based on the Stoner–Wohlfarth model[71,72] taking into account dipolar interactions are performed. A random distribution of the easy axes of nanocrystals is assumed. This is a rough approximation because we know from the reduced
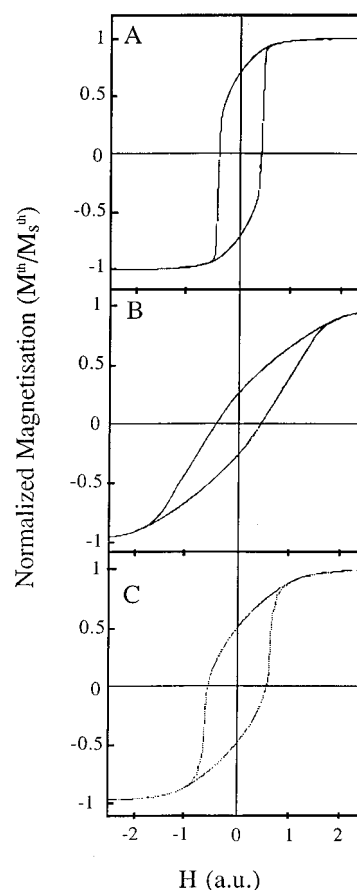

Figure 17. Calculated hysteresis for a hexagonal lattice. (A) $\alpha_d = 0.10$, applied field parallel to the surface. () $\alpha_d = 0.10$, applied field normal to the surface. (C) $\alpha_d = 0$, the case of isolated particles.

remanences of nanocrystals dispersed in liquid that they have cubic anisotropy. From this model, a coupling constant α_d is deduced. It is given by

$$\alpha_d = \frac{\pi}{12} \frac{M_s^2}{K} (D/d)^3$$

where K, D, and d are the anisotropy constant, the particle diameter, and the neighbor distance of nanocrystals, respectively. Hence, the coupling constant, α_d, is determined from the experimental measurements (Table 4).

For various α_d values, the magnetization curves are simulated when the applied field is parallel and perpendicular to the substrate. The hysteresis loops corresponding to $\alpha_d = 0.10$ and the two orientations of the applied field are shown in Figure 17A,B. The non interacting case, $\alpha_d = 0$, corresponding to dispersed particles is also shown (Figure 17C). At a qualitative level, the hysteresis loop is sharper than that corresponding to the isolated particles ($\alpha_d = 0$) when the applied field is parallel to the surface. Conversely, it is smoother and tilted when the applied field is normal to the surface. The nanocrystals are not close enough to reach coercivity due to dipolar interactions alone. The hysteresis loops calculated for the square and the hexagonal lattices with the same value of α_d are very close. Therefore, for a low coupling, the lattice structure has a negligible effect on the magnitude of the deviation of the magnetization due to dipolar interactions. The coupling constant α_d (and thus the packing fraction of the monolayer) appears to be the major parameter for this deviation.

To take into account the presence of vacancies observed in the experimental samples, we performed calculations by intro-

ducing a fraction, f_d, in the lattice of unoccupied sites chosen randomly. For small f_d values, the presence of vacancies in the experimental samples will be taken into account by reducing the coupling constant α_d. Hence, when allowances are made for the nanocrystal vacancies, the effective coupling constant is reduced. For this value, the ratio γ_{theo} of the reduced remanence under perpendicular to parallel applied field is deduced from the simulated hysteresis loop. This value is compared to that obtained from the measured magnetization curves. Table 4 shows rather good agreement between the γ value deduced from experiments, γ_{exp}, and from calculation, γ_{theo}.

From these data, it is concluded that the difference in the hysteresis curves between nanocrystals deposited on a substrate and dispersed in a matrix is mainly due to dipolar interactions between nanocrystals. This is explained in terms of a demagnetizing field effect. From simulation, it is concluded that the precise structure of the lattice is likely to play a negligible role.

Let consider the magnetic properties of the 3D assemblies described on Figure 9.[73] To simplify the text, we called the samples obtained by applying zero (Figure 9A), 0.27 T (Figure 9C), and 0.56 T fields (Figure 9B) A, B, and C, respectively. The hysteresis loops are recorded when the applied magnetic field is parallel to the substrate, i.e., parallel to the film direction. Under these experimental conditions, the nanocrystals form a film and the demagnetizing factor is close to zero. A change in the hysteresis loop with the sample used is observed. The hysteresis loop of sample A is inside that of sample B. Similarly, it is straighter for sample C than for B. The reduced remanences are 0.50, 0.57, and 0.70 for A, B, and C, respectively. The coercive field is 0.27 T for A and B and 0.30 T for C. The increase in the reduced remanence when a magnetic field is applied to the sample during the deposition process cannot be attributed to a change in the macroscopic shape as this remains the same for both B and C. Such behavior could be attributed either to a partial orientation of the easy axes or to the formation of ferromagnetic domains induced by dipolar interactions. When the nanocrystal easy axes are oriented along a given direction, the reduced remanence is expected to be 1 when the applied field is parallel to the axes. If the applied field is perpendicular to the easy axes, the reduced remanence depends on the anisotropy of the material. It is zero for an uniaxial anisotropy and 0.83 for a cubic one. Hence, for cubic anisotropy, the calculated reduced remanence of nanocrystals either having or not having their easy axes oriented, the reduced remanence remains on the same order of magnitude (around 0.85). Cobalt nanocrystals having 5.8[32] and 8 nm[70] as average diameters are both characterized by cubic anisotropy. Because of that, it is impossible to differentiate between an orientation of the easy axes and formation of ferromagnetic domain when a magnetic field is applied during the evaporation process.

III.2.2. Ferrite Nanocrystals.[40,41] The reduced remanence of γFe_2O_3 nanocrystals isolated in a matrix is 0.30 (Table 5). This value is lower than that calculated for uniaxial anisotropy (0.50). This clearly indicates that γFe_2O_3 nanocrystals are characterized by uniaxial anisotropy. The magnetization behavior is compared for γFe_2O_3 nanocrystals deposited on a substrate, as described in II.3.2. The drops remain on the substrate during the evaporation process, and the same amount of nanocrystal is deposited on the substrate. This makes possible comparison of the magnetic behavior of the various samples. For simplicity, samples deposited without applied field (Figure 13B) are denoted A, whereas those obtained under 0.01 T (Figure 13C) and 0.05 and 1.8 T (Figure 13D) are denoted B, C, and D, respectively. The hysteresis curves of ferrite nanocrystals differing in their

TABLE 5: Variation of the Ratio of the Remanence and Saturation Magnetization and the Coercitivity H_c at 3 K of γFe_2O_3 Nanocrystals[a]

samples	powder	isolated particles	A	B	C	D
M_r/M_s	0.23	0.3	0.40	0.44	0.50	0.55
(∥) H_c (Oe)	340	300	300	325	325	340

a The field applied to the substrate is either parallel (∥) or perpendicular(⊥) to the algined particles.
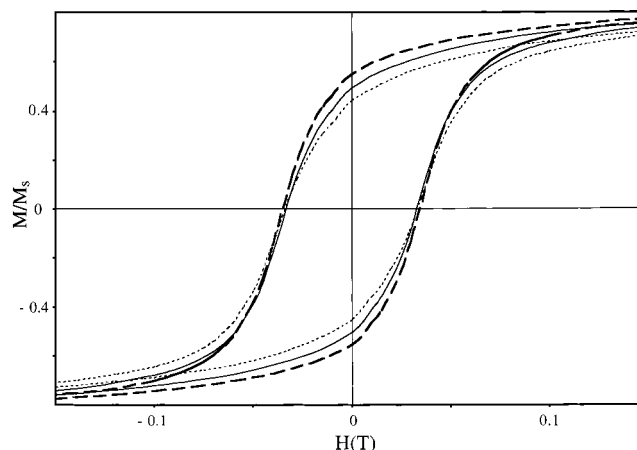

Figure 18. Magnetization curves at 3 K plotted for ferrite nanocrystals deposited on HOPG substrate for samples B (━ ━), C (—), and D (‐ ‐), with the field applied parallel to the aligned particles.

organizations were recorded at 3 K, with the applied field parallel to the alignment of nanocrystals. For all the samples, saturation magnetization (80 emu g^{-1}) is reached at 3 T. This is in good agreement with the value found by Mollard.[74] The reduced remanence (M_r/M_s) and the coercive field are compared under various experimental conditions (Table 5).

When maghemite nanocrystals are deposited randomly on the substrate, the magnetization curve shows a reduced remanence (M_r/M_s) of 0.40, with a coercive field of 300 Oe. When nanocrystals are assembled in ribbons, the hysteresis loops change markedly. They depend on the applied field used during the evaporation process to form ribbons.

All the samples considered (B, C, and D) are ribbons made of nanocrystals. The major difference between these three samples is the value of the applied field used (0.01, 0.05, and 1.8 T, respectively). The shape of the sample remains the same. Figure 18 shows that as the field strength increases during nanocrystal deposition on the substrate, the magnetization curves are straightened, with an increase in the reduced remanence (Table 5). The coercive field is roughly constant ($H_c = 325$ Oe). The hysteresis loop curvature changes, and the two magnetization curves remain located inside that recorded for particles deposited under a field of 1.8 T. When the applied field is perpendicular to the nanocrystals alignment, the hysteresis loop is smother compared to that observed when the applied field is parallel. The hysteresis loop of D is smoother than that obtained with B (Figure 19). As already mentioned, if the easy axes were totally oriented, the hysteresis loop measured when the field is parallel to the easy axes would be expected to be rectangular, whereas under a perpendicular direction, it would be a straight line without coercive field.[82] Such hysteresis loop behavior is observed for C and D. That of D is more pronounced that C with a straightened hysteresis loop when the applied field is parallel to the easy axes and smoother when it is perpendicular. This confirms the partial orientation of the easy magnetic axes.
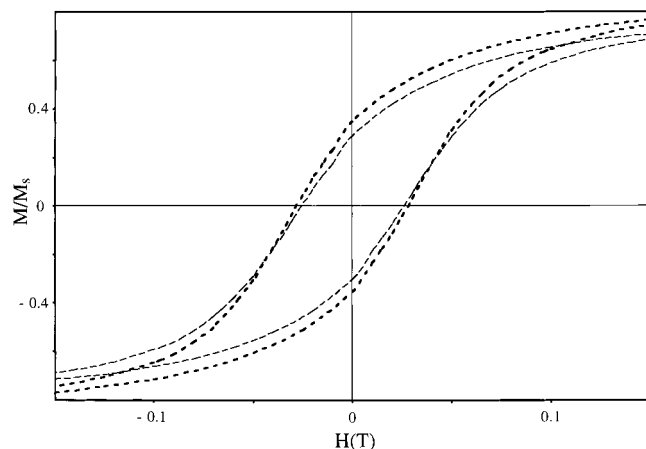
Feature Article

J. Phys. Chem. B, Vol. 105, No. 17, 2001 **3369**

Figure 19. Magnetization curves at 3 K plotted for ferrite nanocrystals deposit on HOPG substrate for samples B (— —) and D (− −), with the field applied perpendicular to the aligned particles.

By taking into account the magnetic susceptibility at low temperature, it is possible to estimate the degree of alignment of the easy magnetic axes of the nanocrystals in a sample. It is found to be close to 80%.[41] From simulation, this value drops to 50%.[75]

In conclusion, the application of a magnetic field during the deposition process makes it possible to partially orient the easy axes of uniaxial nanocrystals along the applied field. The present data described above are obtained wih ferrite coated with nitrate and dispersed in aqueous solution. One of the major differences between these two types of materials is their coating. The orientation of the easy axes along the direction of the applied field involves rotation of the nanocrystals.

IV. Electronic Transport Properties[36]

When a single silver nanoparticle is deposited on a gold 111 substrate, the scanning tunneling spectroscopy measurement indicates a double tunnel junction (Figure 20A). When the applied bias voltage V is increased, the capacitor elements (defined by the tip−particle interface and the particle−substrate interface) are charged (up), and the detected current I is initially close to zero. Above a certain threshold voltage, electrons can tunnel through the interfaces, and the current increases with the applied voltage. A plot of dI/dV versus V (see insert of Figure 20A) clearly shows that the derivative reaches zero at zero V. The nonlinear profile of the $I(V)$ curve and the zero dI/dV at zero bias voltage are characteristic of the well-known Coulomb blockade effect. The voltage range over which there is zero current is ca. 2 V and indicates that the dodecanthiolate ligands on the silver nanocrystals are sufficiently good electrical insulators that they act as tunneling barriers between the particles and the underlying substrate. It is also significant that no Coulomb staircase is observed in Figure 20A. The present STS experimental setup employed a constant current mode, which imposes a tip−particle distance needed to maintain a 1 nA current at a bias voltage of −1 V. The tip−particle distance in this case does not correspond to that needed for the observation of a Coulomb staircase. Since the particle−substrate distance is fixed by the dodecanethiolate coating, both tunnel junctions are characterized by fixed parameters. Similar Coulomb block-ade behavior has been observed elsewhere.[76,77]

Figure 20B shows the $I(V)$ curve for silver nanoparticles self-organized in a 2D superlattice on an Au(111) substrate. For a large voltage bias, both positive and negative, the current is an order of magnitude lower than that observed for isolated
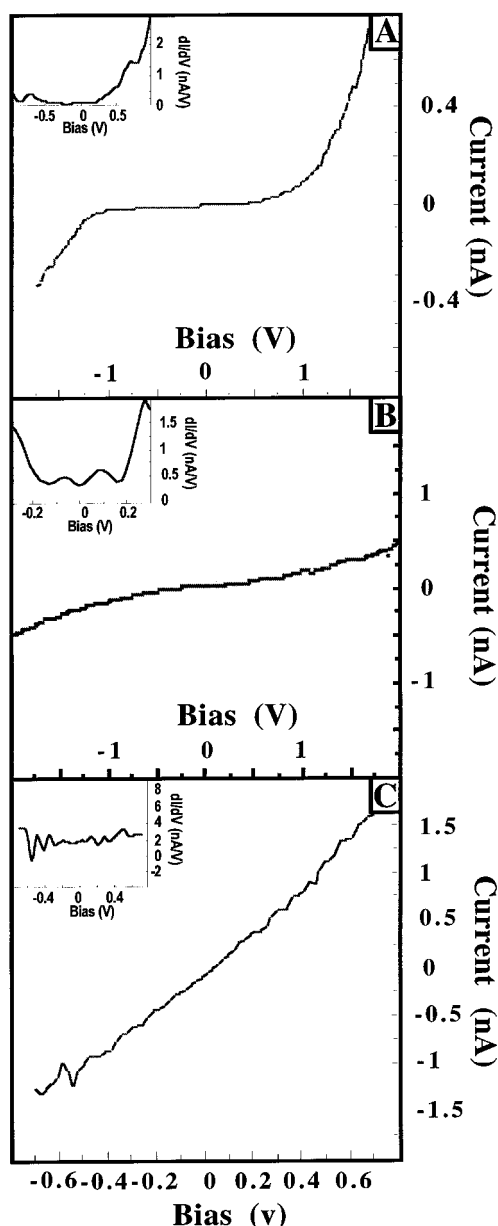

Figure 20. Current−voltage curves for 5 nm diameter silver nano-particles on Au(111) substrate obtained sith STM method. (A) Isolated silver nanocrystal. (B) 2D lattice. (C) FCC supracrystal. Insets in each case are the corresponding derivative curves (dI/dV vs V).

particles. The Coulomb gap is small (ca. 0.45 V, compared to the 2 V seen in the isolated particles), and the overall $I(V)$ curve is more linear than that seen in Figure 20A. This indicates an increase in the ohmic contribution to the current. In other words, the tunneling contribution to the total current decreases, and more conductive pathways between particles are established. The derivative curve shown in the insert of Figure 20B indicates a metallic conduction behavior with dI/d$V \neq 0$ at zero bias voltage. From the $I(V)$ and dI/dV curves, it can be concluded that when the particles are arranged in a 2D lattice, the tunneling current exhibits both metallic and Coulomb contributions. This indicates that lateral tunneling between adjacent particles is very large and contributes to the total electron transport process. The 2D lattice results presented here are in good agreement with data published elsewhere. The $I(V)$ curves for aluminum island structures on aluminum substrates (linked by an Al_2O_3 spacer) were obtained at 40 mK both when they were isolated, and organized in 2D lattices. The $I(V)$ curves they obtained were

different for isolated islands and 2D lattices, with the latter system indicating interisland connections. The Coulomb gap of gold nanocrystals coated with dihexanethiolates (corresponding to a 1.4 ligand barrier) decreases with increasing coverage of the particles on the substrate.[89] Similar properties were found with propanethiolate coated silver nanoparticles; as the monolayer compression reduced the interparticle spacing, the monolayer showed a metallic response to an applied voltage.[79] The difference between these previous results and the present data is that the average interparticle spacing was either not controlled or rather small. In our studies, the average distance between particles is large (1.8−2 nm), and the nanocrystals are self-organized in a close packed hexagonal network. With the ordered packing, lateral electron transport takes place through insulating ligand shells even at these larger distances.

When silver nanocrystals are assembled in a 3D FCC structure, the $I(V)$ curve shows a linear ohmic behavior (Figure 20C). The dI/dV curve is essentially flat, indicating metallic behavior without Coulomb staircases (inset 20C). Note that the voltage scale in Figure 20C is smaller than that in panels A and B of Figure 20. The absolute current in the 3D structure is much higher than that in the isolated silver particle and 2D monolayer structure. The ohmic behavior cannot be attributed to the coalescence of the particles. We have shown through TEM studies that the silver particles remain spherical.[11,20,34] Furthermore, as discussed above, the redispersal of the silver particles in the FCC structure into hexane solution leads to absorption spectra that are virtually the same as the original hexane solutions of silver nanocrystals used to deposit the assemblies. Similar behavior has been observed when HOPG is used as a substrate in place of gold.[20,34]

Thus, we conclude that the FCC structure of the superlattice induces an increase in the tunneling rate via a decrease in resistance between the particles. The electron tunneling between adjacent particles becomes a major contribution to conduction, and the Coulomb blockade effect in the $I(V)$ curves is inhibited. The mechanism may involve an enhanced dipole−dipole interaction along the vertical (z) axis. When subjected to a voltage bias, the Fermi level of the individual nanocrystals is also perturbed. The details remain to be uncovered, but it is clear that a "supra" crystal of coated metal nanoparticles can behave as a metal.

Appendix

1. Synthesis of Silver Sulfide Nanocrystals (1,2,5). Ag_2S nanocrystallites are synthesized by mixing two 0.1 M Na(AOT) micellar solutions (hexane solvent), each having the same water content, but with one containing 8×10^{-4} M sodium sulfide (Na_2S) and the other 8×10^{-4} M (Ag(AOT). Brownian motion leads to collisions between the two types of micelles, and in some events, there is an efficient exchange of water pool contents. After a few minutes, the reaction of Ag^+ and S^{2-} leads to nanosized Ag_2S particles. Significantly, the average size of the particles increases linearly with water content. The standard deviation in the distribution of particle sizes is about 30%, relative to the average size.

Pure alkanethiols, $C_nH_{2n+1}SH$ (where n is an even number varying from 6 to 18), are added (1 μL per ml of micelle solution) to the reverse micelle solutions containing Ag_2S nanocrystals. After evaporation of the solvents at 60 °C, the resulting solid is washed with ethanol and filtered. The silver sulfide nanocrystals coated with the alkanethiols are then dispersed in heptane, forming an optically clear solution. This procedure does not allow for the extraction of the largest particles (ca. 10 nm) from the reverse micelles. Thus, the extraction engenders a size selection resulting in a smaller average diameter as well as a decrease in the relative distribution of sizes from 30% to 14%.

2. Synthesis of Silver Nanocrystals.[11,20] As described above in the case of Ag_2S nanocrystals, the synthesis of Ag nanoparticles involves the mixing of two reverse micelle solutions, each with the water content parameter w ([H_2O]/[AOT]) fixed at 40. The total AOT concentration in the first solution is distributed as 30% Ag(AOT) and 70% Na(AOT). The second solution contains Na(AOT) and 0.07 M hydrazine (N_2H_2). After the solutions are mixed and the Ag particles formed from the reduction of Ag^+ by hydrazine, the addition of dodecanethiol (1 μL per ml of micelle solution) results in the coating of the particles with a dodecanethiolate layer and subsequent flocculation. The solution is then filtered to isolate the particles, which can be easily redispersed in hexane.

After the dodecanethiol extraction step, the size distribution is reduced from ±40% to ±30%. Since the polydispersity is still large at this point, size-selective precipitation (SSP) is employed to reduce the size distribution. SSP is a well-known technique for separating mixtures of copolymers and homopolymers that occur during the synthesis of sequenced copolymers and has also been used for the extraction of nanosized crystals.[80] SSP utilizes a mixture of two miscible solvents, each differing in its ability to dissolve the surfactant alkyl chains. For example, alkanethiolate-coated silver particles are highly soluble in hexane but poorly soluble in pyridine. Thus, pyridine is added in steps to a hexane solution containing coated silver nanoparticles. When the hexane/pyridine volume ratio is about 50%, the solution becomes cloudy, indicating agglomeration of the largest silver particles. The larger particles agglomerate first because of their stronger van der Waals interactions. This solution is centrifuged, and the fraction of solution rich in agglomerate is separated. The resulting supernatant is small particle-rich. The silver particles in the agglomerate-rich fraction can be redispersed via addition of hexane to form a clear solution. By repeating this procedure several times on the supernatant, we can obtain very small particles, with low polydispersity (15%).

3. Synthesis of Cobalt Nanocrystals.[21,32,70] A reverse micellar solution containing 0.25 M Na(AOT) and 0.02 M Co-$(AOT)_2$ is mixed with a 0.25 M Na(AOT) micellar solution also containing 0.02 M sodium borohydride ($NaBH_4$). Both micellar solutions possess the same water content parameter ($w = 10$), which implies a water radius of $R_w = 1.5$ nm.[81] The synthesis is carried out in air. After mixing, the solution remains optically clear, and its color turns from pink to black, indicating the formation of colloidal particles. Under anaerobic conditions, the cobalt particles are extracted from the reverse micelles by covalent attachment of either tri-octyl phosphine[21] or lauric acid[39] and then redispersed in pyridine or hexane, respectively. The covalent attachment based extraction step results in a size selection similar to that seen in the Ag_2S system discussed earlier. The surface modification of the cobalt particles also significantly improves their stability when exposed to air. Cobalt nanoparticles prepared in this manner can be stored without aggregation or apparent oxidation for at least 1 week.

4. Synthesis of Cobalt Ferrite Nanocrystals.[55,56] Normal micellar solutions containing 5.25×10^{-4} M Co$(DS)_2$ and 7×10^{-3} M Fe $(DS)_2$ are mixed and then maintained at 28.5

Feature Article

J. Phys. Chem. B, Vol. 105, No. 17, 2001 **3371**

°C. A 0.44 M solution of dimethylammonium hydroxide ($(CH_3)_2NH_2OH$) is added to the micellar solution while it is vigorously stirred. After 2 h, a magnetic precipitate is observed and subsequently separated from the solution by centrifugation. The precipitate is washed with 0.01 M nitric acid and then redispersed in hexane. A 0.015 M solution of sodium citrate ($Na_3C_6O_7H_5$) is added, and the solution is stirred at 90 °C for 30 min. Acetone is added to precipitate the particles again, and the solid is washed with copious amounts of acetone. After air-drying, the resulting powder of citrate coated cobalt ferrite nanocrystals can be redispersed in aqueous solution. The resulting solution is a neutral magnetic fluid.

References and Notes

(1) Motte, L.; Billoudet, F.; Pileni, M. P. *J. Phys. Chem.* **1995**, *99*, 16425.

(2) Murray, C. B.; Kagan, C. R.; Bawendi, M. G. *Science* **1995**, *270*, 1335.

(3) Ohara, P. C.; Leff, D. V.; Heath, J. R.; Gelbart, W. M. *Phys. Rev. Lett.* **1995**, *75*, 3466.

(4) Brust, M.; Bethell, D.; Schiffrin, D. J.; Kiely, C. *Adv. Mater.* **1995**, *9*, 797.

(5) Motte, L.; Billoudet, F.; Lacaze, E.; Pileni, M. P. *Adv. Mater.* **1996**, *8*, 1018.

(6) Harfenist, S. A.; Wang, Z. L.; Alvarez, M. M.; Vezmar, I.; Whetten, R. L. *J. Phys. Chem.* **1996**, *100*, 13904.

(7) Hostetler, M. J.; Stokes, J. J.; Murray, R. W. *Langmuir* **1996**, *12*, 3604.

(8) Whetten, R. L.; Khoury, J. T.; Alvarez, M. M.; Murthy, S.; Vezmar, I.; Wang, Z. L.; Cleveland, C. C.; Luedtke, W. D.; Landman, U. *Adv. Mater.* **1996**, *8*, 428.

(9) Luedtke, W. D.; Landman U. *J. Phys. Chem.* **1996**, *100*, 13323.

(10) Motte, L.; Billoudet, F.; Lacaze, E.; Douin, J.; Pileni, M. P. *J. Phys. Chem. B* **1997**, *101*, 138.

(11) Taleb, A.; Petit, C.; Pileni, M. P. *Chem. Mater.* **1997**, *9*, 950.

(12) Harfenist, S. A.; Wang, Z. L.; Whetten, R. L.; Vezmar, I.; Alvarez, M. M. *Adv. Mater.* **1997**, 9, 817.

(13) Ohara, P. C.; Heath, J. R.; Gelbart, W. M. *Angew. Chem., Int. Ed. Engl.* **1997**, *36*, 1078.

(14) Vijaya Sarathy, K.; Raina, G.; Yadav, R. T.; Kullkarni, G. U.; Rao, C. N. R. *J. Phys. Chem. B* **1997**, *101*, 9876.

(15) Murthy, S.; Wang, Z. L.; Whetten, R. L. *Philos. Mag. Lett.* **1997**, *75*, 321.

(16) Badia, A.; Cuccia, V.; Demers, L.; Morin, F.; Lennox, R. B. *J. Am. Chem. Soc.* **1997**, *119*, 2682.

(17) Schaff, T. G.; Hafigullin, M. N.; Khoury, J. T.; Vezmar, I.; Whetten, R. L.; Cullen, W. G.; First, P. N.; Gutierrez-Wing, C.; Ascensio, V.; Jose-Ycaman, M. J. *J. Phys. Chem. B* **1997**, *101*, 7885.

(18) Yin, J. S.; Wang, Z. L. *J. Phys. Chem. B* **1997**, *101*, 8979.

(19) Yin, J. S.; Wang, Z. L. *Phys. Rev. Lett.* **1997**, *79*, 2570.

(20) Taleb, A.; Petit, C.; Pileni, M. P. *J. Phys. Chem. B* **1998**, *102*, 2214.

(21) Petit, C.; Taleb, A.; Pileni, M. P. *Adv. Mater.* **1998**, *10*, 259.

(22) Motte, L.; Pileni, M. P. *J. Phys. Chem. B* **1998**, *102*, 4104.

(23) Chung, S. W.; Markovich, G.; Heath, J. R. *J. Phys. Chem. B* **1998**, *102*, 6685.

(24) Korgel, B. A.; Fitzmaurice, D. *Adv. Mater.* **1998**, *10*, 661.

(25) Wang, Z. L.; Harfenist, S. A.; Whetten, R. L.; Bentley, J.; Evans, N. D. *J. Phys. Chem. B* **1998**, *102*, 3068.

(26) Wang, Z. L.; Harfenist, S. A.; Vezmar, I.; Whetten, R. L.; Bentley, J.; Evans, N. D.; Alexander, K. B. *Adv. Mater.* **1998**, *10*, 808.

(27) Vossmeyer, T.; Chung, S.; Gelbart, W. M.; Heath, J. R. *Adv. Mater.* **1998**, *10*, 351.

(28) Fink, J.; Kiely, C. J.; Bethell, D.; Schiffrin, D. *J. Chem. Mater.* **1998**, *10*, 922.

(29) Kiely, C. J.; Fink, J.; Brust, M.; Bethell, D.; Schiffrin, D. J. *Nature* **1998**, *396*, 444.

(30) Brown, L. O.; Hutchison, J. E. *J. Am. Chem. Soc.* **1999**, *121*, 882.

(31) Lin, X. M.; Sorensen, C. M.; Klabunde, K. *J. Chem. Mater.* **1999**, *11*, 198.

(32) Petit, C.; Taleb, A.; Pileni, M. P. *J. Phys. Chem. B* **1999**, *103*, 1805.

(33) Maenosono, S.; Dushkin, C. D.; Saita, S.; Yamaguchi, Y. *Langmuir* **1999**, *15*, 957.

(34) Taleb, A.; Russier, V.; Courty, A.; Pileni, M. P. *Phys. Rev. B* **1999**, *59*, 13350.

(35) Russier, V.; Pileni, M. P. *Surf. Sci.* **1999**, *425*, 313.

(36) Taleb, A.; Silly, F.; Gusev, O.; Charra, F.; Pileni, M. P. *Adv. Mater.* **2000**, *12*, 119.

(37) Petit, C., Cren, T., Roditchev, D., Sacks, W., Klein, J.; Pileni, M. P. *Adv. Mater.* **1999**, *11*, 1358.

(38) Kurrika, V.; Shafi, P. M.; Felner, I.; Mastai, Y.; Gedanken, A. *J. Phys. Chem. B* **1999**, *103*, 3358.

(39) Russier, V.; Petit, C.; Legrand, J.; Pileni, M. P. *Phys. Rev. B* **2000**, *62*, 3910.

(40) Ngo, T.; Pileni, M. P. *Adv. Mater.* **2000**, *12*, 276.

(41) Ngo, T.; Pileni, M. P. *J. Phys. Chem.* **2001**, *105*, 53.

(42) Motte, L.; Lacaze, E.; Maillard, M.; Pileni, M. P. *Langmuir* **2000**, *16*, 3803.

(43) Motte, L. Personnal communication.

(44) Bain, C. D.; Troughton, E. B.; Tao, Y T.; Evall, J.; Whitesides, G. M.; Nuzzo, R. G. *J. Am. Chem. Soc.* **1989**, *111*, 321.

(45) Hostetler, M. J.; Stokes, J. J.; Murray, R. W. *Langmuir* **1996**, *12*, 3604.

(46) Maillard, M.; Ngo, T.; Motte, L.; Pileni, M. P. *Adv. Mater.*, **2001**, *13*, 200.

(47) Maillard, M.; Motte, L.; Pileni, M. P. *J. Phys. Chem.* **2000**, *104*, 11871.

(48) Courty, A.; Araspin, O.; Fermon, C.; Pileni, M. P. *Langmuir* **2001**, *17*, 1372.

(49) Courty, A.; Fermon, C.; Pileni, M. P. *Adv. Mater.* **2001**, *13*, 254.

(50) The log-normal equation is

$$p(s) = \frac{1}{d\sigma_s\sqrt{2\pi}} \exp\left(-\frac{\ln^2 \frac{s}{s_0}}{2\sigma_s^2}\right)$$

where σ_s is the surface area standard deviation and s_0 the mean surface area. The log-normal distribution has the advantage of retaining the diameters (refs 93 and 94) and the surface area with a surface area standard deviation ($\sigma_s = 2\sigma_d$) and a mean surface area $s_0 = \pi d^2$.

(51) Legrand, J.; Ngo, T.; Petit, C.; Pileni, M. P. *Adv. Mater.*, **2001**, *13*, 58.

(52) Flores, G. A.; Liu, J.; Mohebi, M.; Jamasbi, N. *Int. J. Mod. Phys. B* **1999**, *13*, 2093.

(53) Seul, M.; Andelman, D. *Science* **1995**, *267*, 476.

(54) Hong, C. Y.; Horng, H. E.; Jang, I. J.; Wu, J. M.; Lee, S. L.; Yeung, W. B.; Yang, H. C. *Appl. Phys.* **1998**, 677183.

(55) Ngo, T.; Bonville, P.; Pileni, M. P. *Eur. Phys. J.* **1999**, *9*, 583.

(56) Ngo, T.; Bonville, P.; Pileni, M. P. **2001**, *89*, 3370.

(57) Bohren, C. F.; Huffman, D. R. *Absorption and Scattering of Light by Small Particles*; Wiley: New York, 1983.

(58) Charle, K. P.; Frank, F.; Schulze, W. *Ber. Bunsen-Ges. Phys. Chem.* **1984**, *88*, 354.

(59) Mie Ann, G. *Phys.* **1908**, *25*, 377.

(60) Creighton, J. A.; Eaton, D. G. *J. Chem. Soc., Faraday Trans.* **1991**, *2, 87*, 3881.

(61) Hovel, H.; Fritz, S.; Hilger, A.; Kreibig, U.; Vollmer, M. *Phys. Rev. B* **1993**, *48*, 18178.

(62) Persson, B. N. J. *Surf. Sci.* **1993**, *281*, 153.

(63) Ruppin, R. *Surf. Sci.* **1983**, *127*, 108.

(64) Petit, C.; Pileni, M. P. *J. Phys. Chem.* **1993**, *97*, 12974.

(65) Alvarez, M. A.; Khoury, J. T.; Schaaf, T. G.; Shafigullin, M. N.; Vezmar, I.; Whetten, R. L. *J. Phys. Chem. B* **1997**, *101*, 3706.

(66) Yamaguchi, T.; Ogawa, M.; Takahashi, H.; Saito, N.; Anno, E. *Surf. Sci.* **1983**, *129*, 232.

(67) Kennerly, S. W.; Little, J. W.; Warmack, R. J.; Ferrell, T. L. *Phys. Rev. B.* **1984**, *29*, 2926.

(68) Bobbert, P. A.; Leiger, J. V. *Physica A* **1987**, *147*, 115.

(69) Russier, V.; Petit, C.; Legrand, J.; Pileni, M. P. *Appl. Surf. Sci.* **2000**, *164*, 193.

(70) Legrand, J.; Petit, C.; Pileni, M. P. *J. Appl. Sci.* **2000**, *164*, 186.

(71) Stoner, E. C.; Wohlfarth, E. P. *Philos. Trans. R. Soc. London, Ser. A* **1948**, *A240*, 599; reprinted in *IEEE Trans. Magn.* **1991**, *27*, 3475.

(72) Pfeiffer, H. *Phys. Stat. Sol. (a)* **1990**, *122*, 377.

(73) Legrand, J.; Petit, C.; Pileni, M. P. *J. Phys. Chem.*, in press.

(74) Mollard, P.; Germi, P.; Rousset, A. *Physica B* **1977**, *86−88*, 1393.

(75) Russier, V. Personnal communication.

(76) Simon, U. *Adv. Mater.* **1998**, *10*, 1487.

(77) Rimbert, A. J.; Ho, T. R.; Clarke, J. *Phys. Rev. Lett.* **1995**, *74*, 4714.

(78) Ohgi, T.; Sheng, H. Y.; Nejoh, H. *Appl. Surf. Sci.* **1998**, *130*, 919.

(79) Markovich, G.; Collier, C. P.; Heath, J. R. *Phys. Rev. Lett.* **1998**, *80*, 3807.

(80) Wilson, W. L.; Szajowski, P. F.; Brus, L. E. *Science* **1993**, *262*, 1242.

(81) In *Reverse Micelles*; Pileni, M. P., Ed.; Elsevier: New York, 1979.

(82) Chikazumi, S. *Physics of Magnetism*; Wiley: New York, 1964; p 283.